Efficient ultra-broadband low-resolution astrophotonic spectrographs

Pradip Gatkine,[1,*] Greg Sercel[1], Nemanja Jovanovic,[1], Ronald Broeke[2], Katarzyna Ławniczuk[2], Marco Passoni[2], Ashok Balakrishnan[3], Serge Bidnyk[3], Jielong Yin[3], Jeffrey Jewell[4], J. Kent Wallace[4], Dimitri Mawet,[1,4]

[1]*Department of Astronomy, California Institute of Technology, 1200 E. California Blvd., Pasadena, CA 91125, USA*
[2]*Bright Photonics BV, Horsten 1, 5612 AX Eindhoven, The Netherlands*
[3] *Enablence Technologies Inc., 390 March Road, Ottawa, Ontario, Canada K2K 0G7*
[4]*Jet Propulsion Laboratory, 4800 Oak Grove Drive, Pasadena, CA 91109, USA*
[*]*pgatkine@caltech.edu, NASA Hubble Fellow*
https://sites.astro.caltech.edu/ pgatkine/

Abstract:
Broadband low-resolution near-infrared spectrographs in a compact form are crucial for ground- and space-based astronomy and other fields of sensing. Astronomical spectroscopy poses stringent requirements including high efficiency, broad band operation (> 300 nm), and in some cases, polarization insensitivity. We present and compare experimental results from the design, fabrication, and characterization of broadband (1200 - 1650 nm) arrayed waveguide grating (AWG) spectrographs built using the two most promising low-loss platforms - Si_3N_4 (rectangular waveguides) and doped-SiO_2 (square waveguides). These AWGs have a resolving power ($\lambda/\Delta\lambda$) of ~200, free spectral range of ~ 200-350 nm, and a small footprint of ~ 50-100 mm^2. The peak overall (fiber-chip-fiber) efficiency of the doped-SiO_2 AWG was ~ 79% (1 dB), and it exhibited a negligible polarization-dependent shift compared to the channel spacing. For Si_3N_4 AWGs, the peak overall efficiency in TE mode was ~ 50% (3 dB), and the main loss component was found to be fiber-to-chip coupling losses. These broadband AWGs are key to enabling compact integrations such as multi-object spectrographs or dispersion back-ends for other astrophotonic devices such as photonic lanterns or nulling interferometers.

OCIS codes: (080.1238) Array waveguide devices; (130.0130) Integrated optics; (300.6190) Spectrometers; (300.6340) Spectroscopy, infrared; (050.0050) Diffraction and gratings; (350.1260) Astronomical optics; (230.7370) Waveguides; (230.3990) Micro-optical devices.

1. Introduction

Low-resolution spectroscopy is an essential tool in astronomy for a myriad of science cases, particularly where the sources are faint, or rapid spectroscopy is desired. Some of these cases include the characterization of exoplanet atmospheres [1, 2], planetary missions [3–5], and transients such as Gamma-ray bursts, kilonovae, and supernovae [6]. In addition, low-resolution spectroscopy ($\lambda/\delta\lambda \sim 100$, where λ = wavelength, $\delta\lambda$ = spectral resolution element) is typically desirable in massively multiplexed (multi-object or integral-field) spectrographs to accommodate a large number of spectra on a limited detector area, particularly for survey science and high-spatial-resolution spectroscopy. Astronomical applications pose a set of challenging requirements including high throughput, broad operational band, and polarization insensitivity. Further, space-based telescopes require the spectrographs to be highly compact, and multi-object spectroscopy requires the spectrographs to be highly replicable.

On-chip photonic spectrographs are well-suited to address many of these challenges. Photonic spectrographs operate in the single-mode regime and thus, are diffraction-limited instruments.

Further, these on-chip spectrographs are compact and replicable. Unlike conventional bulk optic spectrographs, photonic spectrographs allow design flexibility in terms of routing of light, placement of spectral channels, and filtering of specific lines (e.g.: atmospheric OH-emission lines [7]), thus catering to a diverse set of science cases. Over the last few years, several novel astrophotonic functionalities have been proposed and experimentally demonstrated [8], including photonic-lantern-based wavefront sensing [9], injection of post-coronagraph light into a single-mode fiber [10, 11], photonic interferometry [12], photonic nulling for high-contrast imaging [13, 14], and spectro-astrometry [15]. These implementations tend to have low-order wavelength dependence. Low-resolution astrophotonic spectrographs are highly desirable in significantly enhancing the utility of these implementations by providing on-chip wavelength dispersion.

Arrayed waveguide gratings (AWGs) provide a promising architecture for building astrophotonic spectrographs. In the past, low-resolution AWG spectrographs have been demonstrated but did not satisfy all three requirements (polarization, bandwidth, throughput) that are essential for astronomy. In this paper, we experimentally investigated three broadband low-resolution AWGs using commercial SiN and SiO_2 platforms to achieve high-performance, low-resolution spectroscopy for astronomy. We briefly describe the AWG designs in section 2, discuss the measured performance of the fabricated AWGs in section 3, compare these results in section 4, and lay down future directions in section 5.

2. AWG designs and material platforms

Silicon nitride (Si_3N_4 core, SiO_2 cladding) and Ge-doped-silica (doped SiO_2 core, SiO_2 cladding) have been shown as two promising material platforms for producing low-loss photonic devices in the near-IR [16, 17]. Therefore, we explored these material platforms for constructing the low-resolution AWGs. The key design requirements of the AWGs are described below.

The AWGs are required to operate over a broad band for astronomical applications. We chose to focus on a band spanning 1.2 to 1.65 μm since it approximately spans the astronomical J- and H-bands. This waveband has also been the focus of several astrophotonic technologies thanks to the legacy of the telecommunication industry [18], which makes it the most mature waveband in integrated photonics and thus, ideal for examining the performance limits. The choice of waveband constrains the waveguide geometry to ensure single-mode operation across the entire band. The spectral resolution required was R $\sim$ 200 to ensure both high signal-to-noise-ratio and the wavelength dispersion needed to distinguish chemical species of interest for the science cases described in section 1. The free spectral range (FSR) of the AWGs is designed to be $\sim$ 200 nm to roughly match the span of the astronomical H-band. We further explored an additional design with an FSR of 350 nm for the SiN material to understand potential challenges in scaling these designs to a larger FSR.

In addition, the polarization-dependent shift in wavelength is required to be less than half of the spectral channel separation to ensure that the resolving power degradation for unpolarized light is less than a factor of 2 [19]. However, the polarization dependence requirement can be relaxed by employing off-chip or on-chip broadband polarization splitters and rotators in the future [20].

Waveguide geometry for SiN: For polarization dependence, a near-square SiN waveguide could be used, for instance, as offered by Ligentec (a slight trapezoid measuring 800 nm $\times$ 800 nm). However, this waveguide geometry has high-index contrast ($\sim$ 19%). The advantage of high-index contrast is that the modes are highly confined, thus allowing sharper bends (with $R_{bend} < 100$ μm), and thereby, ultra-compact footprint [21]. The disadvantage of high index contrast is the high differential between the effective index of the waveguide mode and the effective index of the fiber mode, resulting in high fiber-waveguide coupling losses, even with width tapers ($\sim$2.5

dB/facet, [22]). Such losses are prohibitive in astronomy, and hence, further work is needed to optimize the fiber-waveguide tapers for near-square SiN waveguides.

On the other hand, ultra-thin waveguides (height ~ 50 nm) are suitable for low propagation and coupling losses. However, they lead to large polarization-dependent losses and polarization-dependent wavelength shifts in the AWG spectral channels due to the weak confinement factor of the TM mode and large footprint (several cm^2) due to the large radius of curvature needed to minimize bend losses [23].

Given these constraints, we chose a rectangular waveguide geometry (1000×200 nm) for the SiN AWGs in this paper to minimize the losses at the expense of polarization dependence. The SiN AWGs (#1 and #2) were designed for TE mode. Note that some astronomical applications do require polarization-sensitive spectrographs. For instance, the spectro-interferometers (spectrometers to disperse interference fringes) are typically polarization sensitive since the interference fringes are polarization sensitive.

Waveguide geometry for doped-SiO_2: Given the low index contrast of commercially available doped-SiO_2 platform (n_{core} = 1.47 and $n_{cladding}$ = 1.44 gives an index contrast $\Delta = (n_{core}^2 - n_{clad}^2)/2n_{core}^2 = 2\%$), square waveguides do not pose the challenge of a large index step between the waveguide and fiber modes, thus allowing a high fiber-to-waveguide coupling efficiency. Therefore, we use a waveguide geometry of $3.4 \times 3.4\ \mu m$, to ensure polarization symmetry.

Fabrication: With the waveguide geometries and target resolving power as described above, the properties of the as-designed AWGs are summarized in Table 1. Mask designs of the AWGs are shown in Fig. 1. The AWGs presented here have a large FSR, and hence, require a small differential length (= grating order $\times\ \lambda$) between the arrayed waveguides. Such small differential lengths can be accommodated in multiple ways. For low-index-contrast platforms (such as doped-SiO_2) with large bend radii, the banana shape (Fig. 1-bottom) is the most suitable solution for the AWG geometry. For high-index-contrast platforms (such as SiN), where small bending radii are feasible, a folded architecture can be implemented. A folded architecture allows arbitrarily small differential lengths between a large number of arrayed waveguides in a compact form factor. This architecture is used for AWGs #1 and #2 (Fig. 1: top and middle).

The footprints of AWGs #1 (SiN FSR = 180 nm), #2 (SiN FSR = 350 nm), and #3 (doped-SiO_2 FSR = 200 nm) are 11.75×5.2 mm^2, 11.75×9.2 mm^2, and 11×3.5 mm^2. The SiN AWG was fabricated by Lionix International. The base SiO_2 cladding is grown thermally on the silicon substrate followed by low-pressure chemical vapor deposition (LPCVD) deposition of SiN layer (200 nm). The AWG mask is imprinted using UV contact lithography, followed by dry etching and photoresist removal. Finally, a top layer of cladding is deposited using plasma-enhanced chemical vapor deposition (PECVD). The doped-SiO_2 AWG was fabricated by Enablence. A Ge-doped silica (core) layer of 3.4 μm thickness was deposited on top of a 15 μm thick thermally grown SiO_2 layer. UV stepper lithography was used to imprint the AWG pattern, followed by dry etching and resist removal. Finally, a SiO_2 top cladding layer of 20 μm thickness was deposited.

3. Results and Discussion

3.1. Characterization setup

The input and output waveguides of AWG#1 and AWG#3 were packaged using a polarization-maintaining (PM) fiber array. The input waveguide of the AWG #2 was packaged with PM fiber and the outputs were packaged with an SMF28 fiber array. The polarization-maintaining fiber of choice was Thorlabs PM1300-XP, which is specified across 1270-1625 nm. The input fiber for the AWG was connected to one of two super luminescent diodes (Thorlabs S5FC1018P for 1200-1400 nm and S5FC1005P for 1400-1650 nm). The output fiber of the AWG was connected to an optical spectrum analyzer (OSA) to analyze the output as a function of wavelength. A

Table 1. Summary of the characteristics of the broadband low-resolution AWGs.

	AWG#1	AWG#2	AWG#3
Material platform	Si_3N_4	Si_3N_4	Doped-SiO_2
Waveguide Geometry	1000x200 nm	1000x200 nm	3400x3400 nm
Effective index	TE: 1.58, TM: 1.5	TE: 1.58, TM: 1.5	TE and TM: 1.49
Min. R_{curve}	500 μm	500 μm	1500 μm
Channel Spacing ($\Delta\lambda$)	7.5 nm	8 nm	8.75 nm
Central wavelength	1550 nm	1550 nm	1550 nm
Resolving power ($\lambda/\Delta\lambda$)	200	190	175
FSR	180 nm	350 nm	200 nm
Footprint	11.75×5.2 mm^2	11.75×9.2 mm^2	11×3.5 mm^2

fiber-to-fiber response is measured as a reference for source power, which is then used to derive the overall transmission response of the fiber-chip-fiber system. Note that while AWGs #1 and #2 are designed for TE mode only, we measure and report their performance for both TE and TM modes for complete characterization and comparison.

3.2. Transmission response and throughput

The overall transmission of AWGs #1, #2, and # 3 (including fiber-chip coupling) is shown in figures 2, 3, and 4, respectively. In each figure, the top row shows the TE transmission response and the bottom row shows the TM transmission response across 1200-1400 nm and 1400-1650 nm wavebands. The dotted line at the top indicates 0 dB (100%) transmission. The spectral channels are shown in different colors. The black trace shows a representative spectral channel for reference and helps visualize the FSR. The observations are summarized below.

SiN AWGs: From the transmission profiles of the spectral channels in figures 2 (AWG #1) and 3 (AWG #2), it is clear that these AWGs are broadband and operate over a waveband of 1200-1650 nm, albeit with degradation in throughput and/or crosstalk in certain regions depending on the polarization. For the TE mode in both AWG #1 and #2, the peak transmission of ∼ -3 to -3.5 dB occurs around 1450 nm (see Figures 2, 3, and 5). The transmission rapidly declines at longer wavelengths and flattens out at shorter wavelengths up to 1225 nm (to a level of -7 dB for AWG #1 and -10 dB for AWG #2). On the other hand, for the TM mode in AWGs #1 and #2, a roughly monotonic rise is seen in transmission from 1200 nm to 1650 nm.

For a qualitative investigation of the loss components, we estimated the wavelength-dependent propagation and coupling losses of AWG #1. To do that, we measured the fiber-waveguide-fiber transmission for two reference waveguides with different lengths on a chip (from the same wafer and process batch as AWGs #1 and #2). Both the inputs and outputs of these reference waveguides were packaged on the same side of the chip using a V-grove, and hence, we assumed identical coupling loss for both reference waveguides. With this assumption, we used the difference in

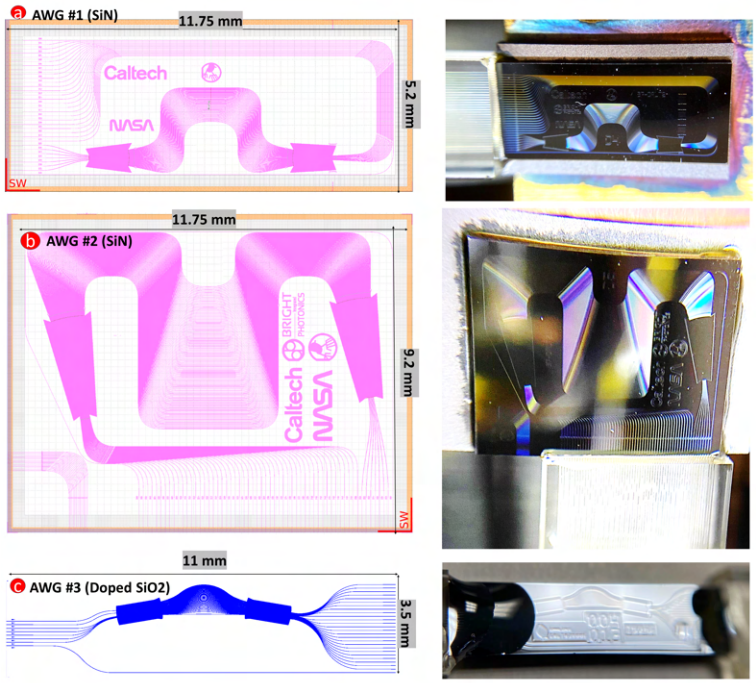

Fig. 1. The CAD profiles and images of each AWG. AWG #1 is the top row (11.75 mm × 5.2 mm), AWG #2 is the middle row (11.75 mm × 9.2 mm), and AWG #3 is at the bottom (11 mm × 3.5 mm).

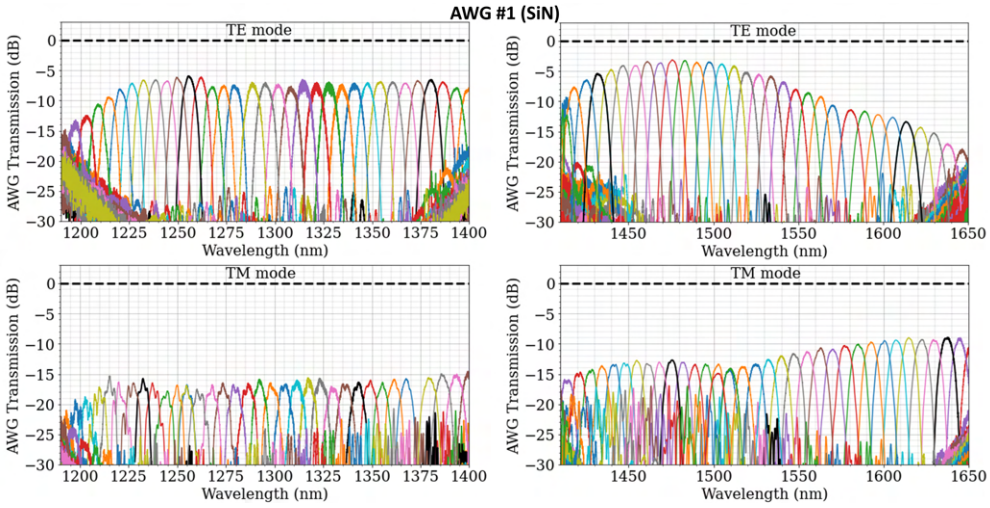

Fig. 2. Broadband and polarization-dependent transmission of AWG #1 (SiN platform). **Top Left:** TE mode transmission response in 1200-1400 nm range. **Top Right:** TE mode transmission response in 1400-1600 nm range. **Bottom Left:** TM mode transmission response in 1200-1400 nm range. **Bottom Right:** TM mode transmission response in 1400-1600 nm range.

reference waveguide transmission to estimate the propagation loss as a function of wavelength.

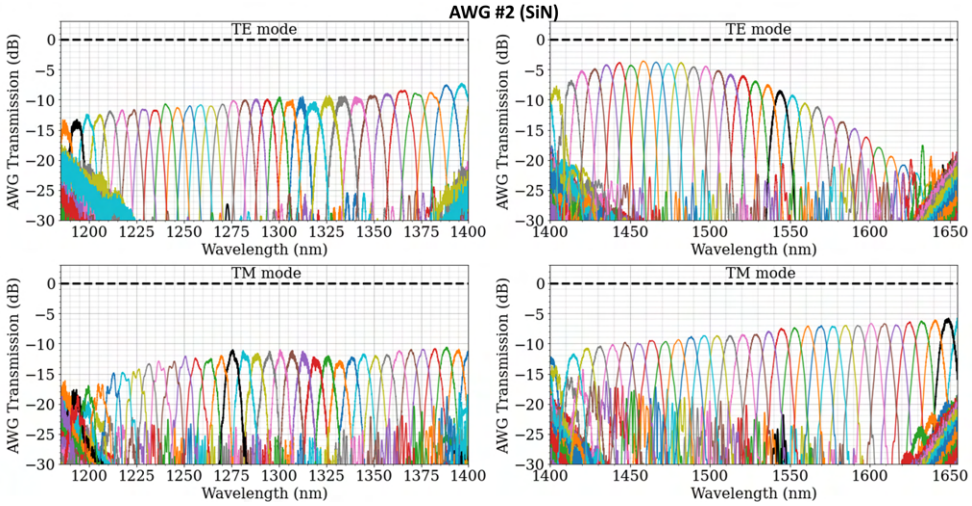

Fig. 3. Broadband and polarization-dependent transmission of AWG #2 (SiN platform). **Top Left:** TE mode transmission response in 1200-1400 nm range. **Top Right:** TE mode transmission response in 1400-1600 nm range. **Bottom Left:** TM mode transmission response in 1200-1400 nm range. **Bottom Right:** TM mode transmission response in 1400-1600 nm range.

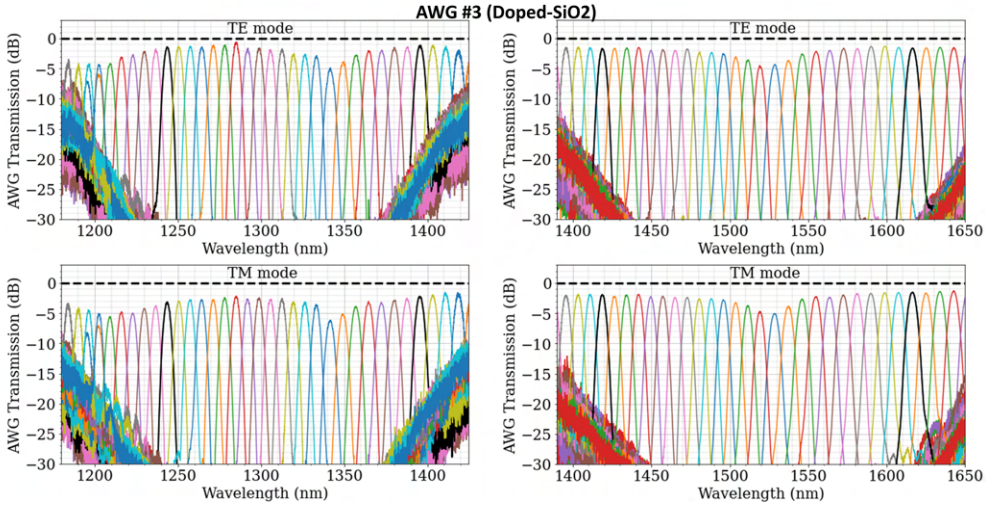

Fig. 4. Broadband and polarization-dependent transmission of AWG #3 (SiO2 platform). **Top Left:** TE mode transmission response in 1200-1400 nm range. **Top Right:** TE mode transmission response in 1400-1600 nm range. **Bottom Left:** TM mode transmission response in 1200-1400 nm range. **Bottom Right:** TM mode transmission response in 1400-1600 nm range.

By applying this propagation loss to the reference waveguide on AWG #1 chip, we estimated the coupling loss as a function of wavelength. This decomposition is shown in Fig. 6.

In Fig. 6, the total reference waveguide loss (fiber-waveguide-fiber) is shown in blue, the total coupling loss (of both facets) is shown in orange, and the total propagation loss is shown in green. The faint bands around the traces indicate the uncertainty. The AWG transmission loss is shown with black points. The transmission loss for AWG #1 in the TM (1200 - 1650 nm) and TE modes (at λ < 1525 nm) is primarily contributed by the coupling loss between fiber-to-waveguide, as

shown in Fig. 6. Coupling loss shown in Fig. 6 includes the loss at both input and output facets. The TM mode transmission as a function of wavelength for AWG #2 can also be explained by the coupling loss given the same material platform and waveguide geometry as AWG #1. Note that there is no anti-reflective (AR) coating on either the fiber or chip facets. AR coating on all the facets will help minimize the Fresnel reflection losses and, thereby, the coupling losses.

However, the rapid decline in the transmission of AWGs #1 and #2 for $\lambda > 1525$ nm in the TE mode cannot be explained by the coupling loss since the coupling loss component is only $\sim$ 1 dB. In addition, for AWG #2, in the TE mode, the downward slope at $\lambda > 1525$ nm is higher compared to AWG #1 (as seen in Fig. 5). The only dissimilar elements that could introduce a differential loss between the two AWGs are the propagation losses and the intrinsic insertion loss of the grating (light lost into neighboring spatial orders, not sampled by the output waveguides [24]). Note that the waveguide-to-slab and slab-to-waveguide interfaces are the same in both AWGs, and would thus yield the same loss in both. As such, the propagation loss in these SiN waveguides is minimal, as shown in Fig. 6. Thus, it is highly likely that the additional loss at longer wavelengths is due to the intrinsic loss of the grating. This needs to be further investigated through extensive simulations and measurement techniques, such as optical backscatter reflectometry [25], to pinpoint the source of this loss, but this is beyond the scope of this paper.

The typical crosstalk observed for both AWGs #1 and #2 in the TE mode is 12-14 dB at λ = 1225-1550 nm and 10 dB at λ = 1550-1600 nm. For the TM mode, the crosstalk is 12-13 dB at λ = 1550-1650 nm and degrades to 5-10 dB at λ = 1225-1550 nm due to significant side lobes from non-adjacent channels in the TM mode.

SiO_2 AWG: The transmission response of the SiO_2 AWG (AWG #3) is shown in Figures 4 and 5 (bottom pannel). It is clear that this AWG is broadband and operates over a waveband of 1200-1675 nm without significant degradation in either polarization. The peak throughput in the TE mode is $\sim$ 1 dB (at 1400 and 1275 nm) and 1.5 dB in the TM mode (at 1415 and 1610 nm). For both TE and TM modes in AWG #3, we observe the typical quasi-Gaussian envelopes of the distinct spectral orders (e.g., 1350 to 1540 nm) that result from the far field electric field distribution of the waveguide geometry at the array-to-output-FPR interface, projected on the AWG's output Rowland circle [24]. Unlike AWGs #1 and #2, the transmission in AWG #3 is more uniform across the entire 1200-1650 nm range without significant losses at shorter or longer wavelengths in excess of this envelope. The non-uniformity loss (difference between central and edge channels in a spectral order envelope) is $\sim$3.5 dB for both TE and TM modes.

Note that in Fig. 4, at $\lambda < 1200$ nm, we see spatial wrapping. The next spatial order at the output FPR of the AWG starts to get sampled by the output waveguides, thus we get the constructive interference of the same wavelength at two different output waveguides. Therefore, we define the operational band only down to 1200 nm. This operational waveband can be expanded in the future by increasing the spatial separation between the spatial orders, which can be accomplished by increasing the ratio of the radius of curvature of the free propagation region and the waveguide spacing of the arrayed waveguides [26].

The crosstalk observed for both TE and TM modes 25-30 dB across λ = 1225-1650 nm with better crosstalk ($\sim$ 30 dB) at λ = 1200-1400 nm and slightly worse ($\sim$ 25-27 dB) at λ = 1400-1650 nm. This suggests that the phase errors in the SiO_2 chip are minimal ($< 60°$), thus minimizing the sidelobes, and improving the noise floor contributed by the adjacent and non-adjacent channels [22].

3.3. Resolving power and FSR

In astronomical spectroscopy, the 3-dB resolving power is defined as $\lambda/\delta\lambda$ where $\delta\lambda$ is the 3-dB width of the spectral channel. We used this definition to estimate the 3-dB resolving powers of each of the fabricated AWGs. It is plotted as a function wavelength in Figure 7. The typical 3-dB

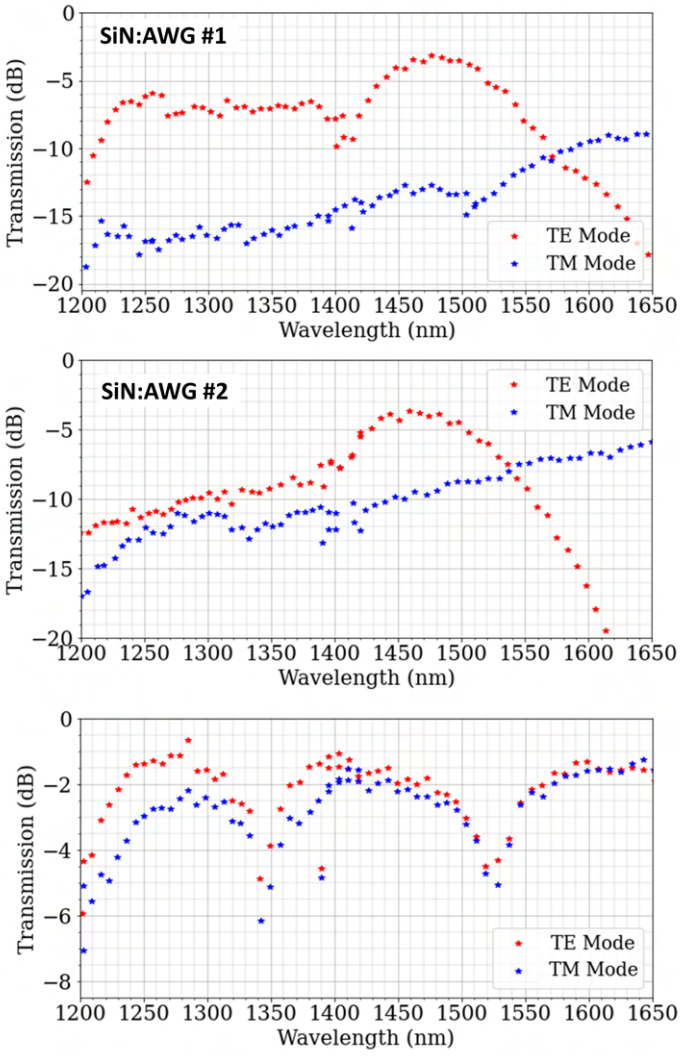

Fig. 5. TE and TM mode transmission responses across the 1200-1650 nm range for SiN-AWG #1 (**top**), SiN-AWG #2 (**middle**), SiO_2-AWG #3 (**bottom**).

resolving power of AWGs #1 and #2 remains in the range of 150-200 across the entire waveband of 1200-1650 nm without a significant difference between TE and TM modes. This is consistent with their target resolving powers. The median 3-dB resolving power of AWG #3 is between 225 to 275 across the entire operational waveband (1175-1675 nm) with identical performance for both polarizations. Note that the channel spacing of AWG #3 is consistent with the target of 8.8 nm. The 3-dB width of these channels ($\delta\lambda$) is narrower than the channel spacing due to sharply defined peaks. Therefore, the 3-dB resolving power is higher. The sharply defined peaks suggest negligible phase errors (as also deduced in section 3.2) [22] and, thereby, negligible spectral channel broadening (i.e., negligible degradation of spectral resolution).

The FSR is given by λ/(grating spectral order), and hence the wavelength dependence is expected. The FSR for AWG #1 for the TE (TM) mode is 123 nm (110 nm) at $\lambda \sim 1300$ nm and 182 nm (162 nm) at $\lambda \sim 1550$ nm. Note that the TM mode values are mentioned in parentheses.

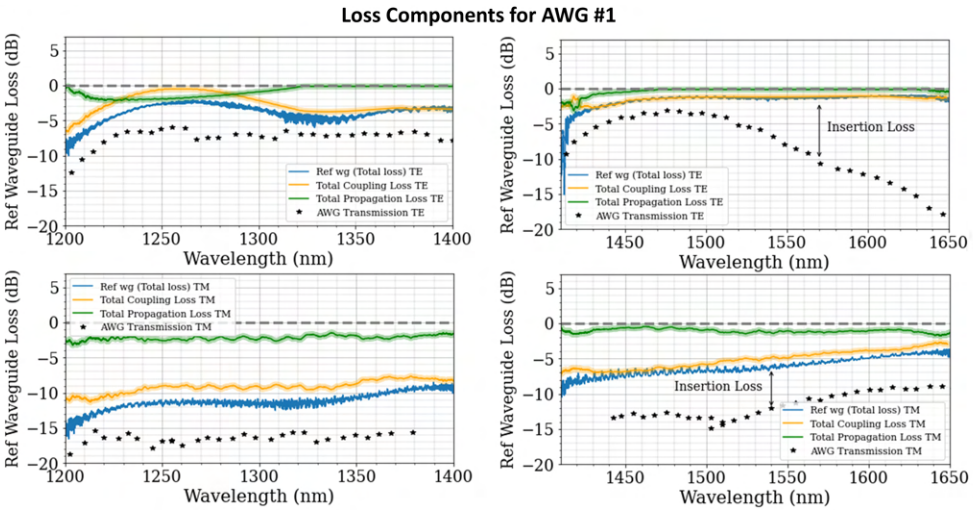

Fig. 6. TE and TM mode transmission responses across the 1200-1650 nm range for a reference SiN waveguide with length comparable to AWG #1. The top panel shows TE polarization response and the bottom panel shows TM polarization response.

For AWG #2, a single spectral order covers much of the operational waveband, with an FSR of 355 nm in TE mode and 375 nm in TM mode across 1200-1650 nm. For AWG #3, the TE and TM mode profiles are nearly identical, thus giving an FSR of 150 nm at $\lambda \sim 1300$ nm and 195 nm at $\lambda \sim 1550$ nm for both TE and TM modes. All the observed FSR values match the design FSR.

3.4. Polarization dependence

Note that the SiN AWGs (AWGs #1 and #2) were optimized for the TE mode and constructed using rectangular waveguides (1000×200 nm). Therefore, a strong form birefringence is expected in these AWGs. We still study their polarization dependence for the sake of completeness. The measured polarization-dependent wavelength shifts are shown in Fig. 8. Both AWG #1 and #2 show a polarization-dependent wavelength shift of $\sim 85 - 90$ nm. This is greater than the expected polarization-dependent shift as calculated from $\Delta n_{eff} \times \lambda_{TE}/n_{eff,TE} = 78.5$ nm at $\lambda = 1550$ nm [26]. This is potentially due to the difference between the refractive indices of PECVD-deposited top cladding and thermally grown bottom cladding and needs further investigation beyond the scope of this paper.

The SiO_2 AWG (AWG #3) is constructed using square waveguides, and hence, is expected to have negligible form birefringence. Indeed, as seen in Figs. 4 and 8, the polarization-dependent shift (PDλ) is < 0.5 nm, which is negligible compared to the resolution element (i.e., FWHM of 6.22 nm at 1550 nm). Thus, there is no degradation in the resolving power with an unpolarized light source (which is typically the case in astronomy). This AWG has a polarization-dependent loss (PDL) of $\sim$1 dB (at $\lambda < 1400$ nm). However, the PDL requirement in astronomy is less stringent compared to PDλ.

4. Conclusion and Future Work

In this paper, we experimentally examined the broadband performance of three low-resolution ($R \sim 200$) AWGs fabricated using commercial foundries. This exploration is centered around the application for on-chip astronomical spectroscopy. AWG #1 (FSR: 180 nm) and #2 (FSR: 350 nm) were built using rectangular Si_3N_4 waveguides, and AWG #3 (FSR: 200 nm) was constructed using square-shaped doped-SiO_2 waveguides. We investigated the transmission

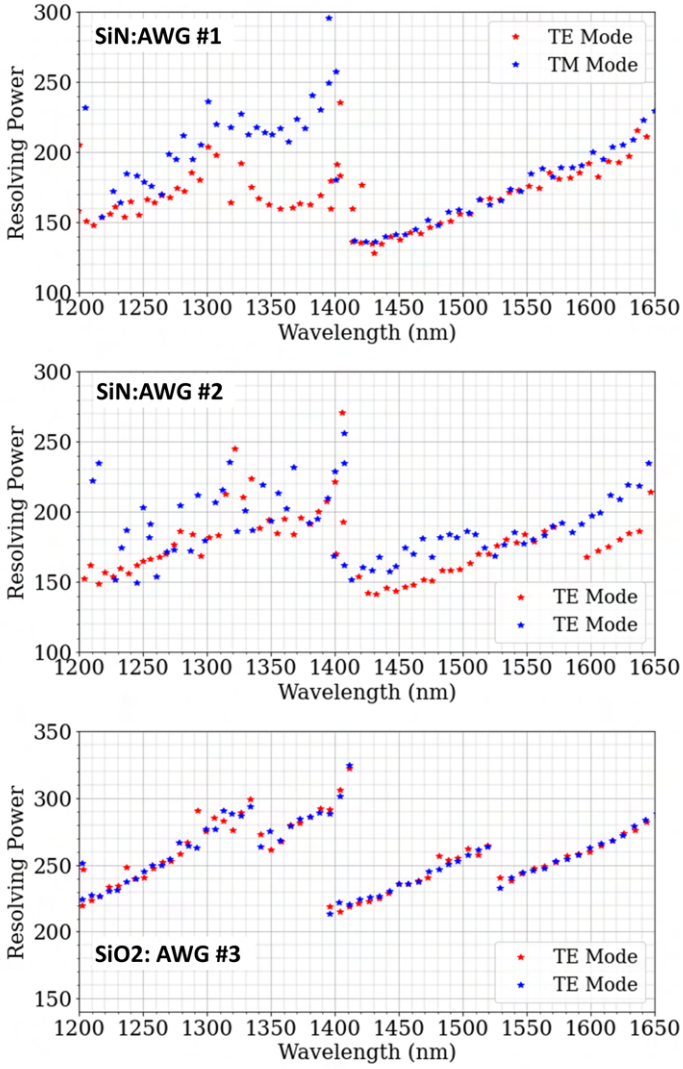

Fig. 7. TE and TM mode resolving power across the 1200-1650 nm range for SiN-AWG #1 (**top**), SiN-AWG #2 (**middle**), SiO2-AWG #3 (**bottom**).

response, resolving power, FSR, and polarization dependence of these AWGs as a function of wavelength. We observed that all three AWGs worked over a broad band (1200 − 1650 nm) for both TE and TM polarizations.

The peak throughput for AWGs #1 and #2 was ∼ 3.5 dB, and for AWG #3 was ∼ 1 dB for the TE mode. The resolving power obtained was close to the design resolving power for all the AWGs. The PDλ was large for AWGs #1 and #2 (∼ 80 nm), which was expected due to their rectangular shape and since they were designed for the TE mode. At the same time, the PDλ was found to be negligible for doped-SiO_2 waveguides, thanks to their square shape.

Considering the fiber-chip coupling losses, broadband low-loss performance, low crosstalk, and polarization-insensitive performance, we find that doped-SiO_2 is an ideally suited platform for low-resolution, broadband on-chip astrophotonic spectroscopy in the astronomical J and H bands (1100-1700 nm). For the SiN platform, the key challenges to be addressed are coupling

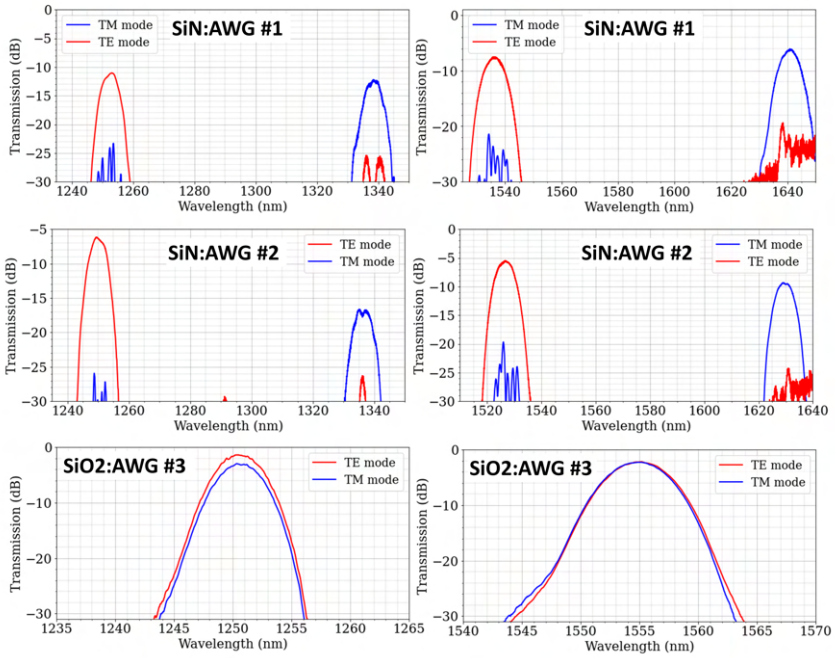

Fig. 8. Polarization dependence of the 3 chips around 1250 nm and 1550 nm for SiN-AWG #1 (**top row**), SiN-AWG #2 (**middle row**), SiO2-AWG #3 (**bottom row**).

losses over a broad band and polarization sensitivity. The coupling losses can be alleviated by adding AR coatings to the fiber and chip facets to minimize the Fresnel reflection losses. In addition, optimizing the tapers to lower the effective index at the waveguide facet and using ultra-high numerical aperture fibers can result in better mode matching, and, thus, minimal coupling losses [27]. For a high-efficiency fiber-waveguide coupling in SiN across 1200−1700 nm, efficient spot-size converters, such as those proposed by [28] and [29] need to be experimentally demonstrated over a broad band. The polarization sensitivity can be resolved by using near-square waveguides (such as those offered by Ligentec) or by employing off-chip or on-chip broadband polarization splitters and rotators in the future [20].

However, there are still further developments that need to be undertaken with the doped-SiO_2-based AWGs before they are employed for astronomical spectroscopy. Since astronomical sources are extremely faint, collecting light from the entire waveband without any gaps is crucial. Thus, the spectral dropout in between neighboring spectral channels needs to be minimized (see Fig. 2 in [22] for more details). This can be done by constructing the channel profiles such that the neighboring channels overlap at their 3-dB point. The current SiO_2 AWG was not designed for this specification, and thus, the neighboring channels overlap at ~6-dB point at 1550 nm, leading to a net spectral dropout of 3 dB (= 6 dB - 3 dB). In addition, achieving the spectral dispersion on a flat focal plane, instead of a Rowland circle in conventional AWGs, allows dicing of the AWG along the focal plane. This enables imaging of the entire focal plane on the detector without any discretization or losses due to sampling by output waveguides and is, thus, useful in astronomy. This can be achieved using a three-stigmatic-point AWG design (as previously shown in [17, 30, 31]).

In addition, the non-uniformity loss of the AWG (the difference between the throughputs at the central and edge channels) needs to be minimized. For AWG #3, it is about 2.5-3 dB. The non-uniformity loss happens due to the far-field illumination pattern of the waveguide at the interface

of the waveguide array and output slab. To minimize the non-uniformity loss, the waveguide geometry at the interface needs to be optimized for a flatter far-field illumination pattern. This can be achieved in the future by introducing nanowire waveguides at the slab-waveguide interface [32], among other approaches. Finally, the AWG FSR needs to be extended from the current 200 nm to at least ~ 300 nm to entirely cover the astronomical J-band (1100-1350 nm) or H-band (1400-1700 nm) without cross-dispersion. Such low-loss, broadband, low-resolution on-chip astrophotonic spectrographs could prove to be a valuable technology for various capabilities such as spectroscopy of directly imaged exoplanets, spectro-interferometry, spectro-astrometry, and so on for the upcoming space-based Habitable Worlds Observatory.

Funding

Support for P Gatkine was provided by NASA through the NASA Hubble Fellowship Grant HST-HF2-51478.001-A awarded by the Space Telescope Science Institute, which is operated by the Association of Universities for Research in Astronomy, incorporated, under NASA Contract NAS5-26555. This work was supported by the Wilf Family Discovery Fund in Space and Planetary Science, funded by the Wilf Family Foundation, as well as the support from Keck Institute for Space Studies at Caltech. Some of this research was carried out at Caltech and the Jet Propulsion Laboratory and funded through the President's and Director's Research & Development Fund program. This work was supported by NASA through the Center Innovation Fund.

Acknowledgments

The authors would like to thank the staff at Lionix for the development of some of the photonics presented herein.

Disclosures

The authors declare no conflicts of interest.

References and links

1. A. S. Burrows, "Spectra as windows into exoplanet atmospheres," Proceedings of the National Academy of Sciences **111**, 12601–12609 (2014).
2. M. R. Swain, P. Deroo, C. A. Griffith, G. Tinetti, A. Thatte, G. Vasisht, P. Chen, J. Bouwman, I. J. Crossfield, D. Angerhausen *et al.*, "A ground-based near-infrared emission spectrum of the exoplanet hd 189733b," Nature **463**, 637–639 (2010).
3. F. E. DeMeo, R. P. Binzel, S. M. Slivan, and S. J. Bus, "An extension of the bus asteroid taxonomy into the near-infrared," Icarus **202**, 160–180 (2009).
4. T. Kohout and A. Näsilä, "Miniaturized spectral imaging instrumentation for planetary exploration," Tech. rep., Copernicus Meetings (2020).
5. C. Lantz, F. Poulet, D. Loizeau, L. Riu, C. Pilorget, J. Carter, H. Dypvik, F. Rull, and S. C. Werner, "Planetary terrestrial analogues library project: 1. characterization of samples by near-infrared point spectrometer," Planetary and Space Science **189**, 104989 (2020).
6. M. Shahbandeh, E. Hsiao, C. Ashall, J. Teffs, P. Hoeflich, N. Morrell, M. Phillips, J. Anderson, E. Baron, C. Burns *et al.*, "Carnegie supernova project-ii: near-infrared spectroscopy of stripped-envelope core-collapse supernovae," The Astrophysical Journal **925**, 175 (2022).
7. T. Zhu, Y. Hu, P. Gatkine, S. Veilleux, J. Bland-Hawthorn, and M. Dagenais, "Arbitrary on-chip optical filter using complex waveguide Bragg gratings," Applied Physics Letters **108**, 101104 (2016).
8. N. Jovanovic, P. Gatkine, N. Anugu, R. Amezcua-Correa, R. Basu Thakur, C. Beichman, C. Bender, J.-P. Berger, A. Bigioli, J. Bland-Hawthorn *et al.*, "2023 astrophotonics roadmap: pathways to realizing multi-functional integrated astrophotonic instruments," Journal of Physics: Photonics (2023).
9. B. R. Norris, J. Wei, C. H. Betters, A. Wong, and S. G. Leon-Saval, "An all-photonic focal-plane wavefront sensor," Nature Communications **11**, 5335 (2020).
10. J.-R. Delorme, N. Jovanovic, D. Echeverri, D. Mawet, J. Kent Wallace, R. D. Bartos, S. Cetre, P. Wizinowich, S. Ragland, S. Lilley *et al.*, "Keck planet imager and characterizer: a dedicated single-mode fiber injection unit

for high-resolution exoplanet spectroscopy," Journal of Astronomical Telescopes, Instruments, and Systems **7**, 035006–035006 (2021).
11. D. Echeverri, J. Xuan, N. Jovanovic, G. Ruane, J.-R. Delorme, D. Mawet, B. Mennesson, E. Serabyn, J. K. Wallace, J. Wang *et al.*, "Vortex fiber nulling for exoplanet observations: implementation and first light," Journal of Astronomical Telescopes, Instruments, and Systems **9**, 035002–035002 (2023).
12. L. Jocou, K. Perraut, A. Nolot, J.-P. Berger, T. Moulin, P. Labeye, S. Lacour, G. Perrin, J.-B. Lebouquin, H. Bartko *et al.*, "The gravity integrated optics beam combination," in "Optical and Infrared Interferometry II," , vol. 7734 (SPIE, 2010), vol. 7734, pp. 1109–1120.
13. F. Martinache and M. J. Ireland, "Kernel-nulling for a robust direct interferometric detection of extrasolar planets," Astronomy & Astrophysics **619**, A87 (2018).
14. B. R. Norris, N. Cvetojevic, T. Lagadec, N. Jovanovic, S. Gross, A. Arriola, T. Gretzinger, M.-A. Martinod, O. Guyon, J. Lozi *et al.*, "First on-sky demonstration of an integrated-photonic nulling interferometer: the glint instrument," Monthly Notices of the Royal Astronomical Society **491**, 4180–4193 (2020).
15. Y. J. Kim, S. Sallum, J. Lin, Y. Xin, B. Norris, C. Betters, S. Leon-Saval, J. Lozi, S. Vievard, P. Gatkine *et al.*, "Spectroastrometry with photonic lanterns," in "Ground-based and Airborne Instrumentation for Astronomy IX," , vol. 12184 (SPIE, 2022), vol. 12184, pp. 1391–1402.
16. D. J. Blumenthal, R. Heideman, D. Geuzebroek, A. Leinse, and C. Roeloffzen, "Silicon nitride in silicon photonics," Proceedings of the IEEE **106**, 2209–2231 (2018).
17. A. Stoll, K. Madhav, and M. Roth, "Design, simulation and characterization of integrated photonic spectrographs for astronomy II: low-aberration generation-II AWG devices with three stigmatic points," Optics Express **29**, 36226–36241 (2021).
18. X. Chen, M. M. Milosevic, S. Stanković, S. Reynolds, T. D. Bucio, K. Li, D. J. Thomson, F. Gardes, and G. T. Reed, "The emergence of silicon photonics as a flexible technology platform," Proceedings of the IEEE **106**, 2101–2116 (2018).
19. P. Gatkine, S. Veilleux, Y. Hu, J. Bland-Hawthorn, and M. Dagenais, "Towards a multi-input astrophotonic AWG spectrograph," in "Advances in Optical and Mechanical Technologies for Telescopes and Instrumentation III," , vol. 10706 (International Society for Optics and Photonics, 2018), vol. 10706, p. 1070656.
20. Y. Xu and J. Xiao, "Ultracompact and high efficient silicon-based polarization splitter-rotator using a partially-etched subwavelength grating coupler," Scientific reports **6**, 27949 (2016).
21. P. Gatkine, N. Jovanovic, J. Jewell, J. K. Wallace, and D. Mawet, "An on-chip astrophotonic spectrograph with a resolving power of 12,000," in "UV/Optical/IR Space Telescopes and Instruments: Innovative Technologies and Concepts X," , vol. 11819 (SPIE, 2021), vol. 11819, pp. 171–180.
22. P. Gatkine, N. Jovanovic, C. Hopgood, S. Ellis, R. Broeke, K. Ławniczuk, J. Jewell, J. K. Wallace, and D. Mawet, "Potential of commercial SiN MPW platforms for developing mid/high-resolution integrated photonic spectrographs for astronomy," Applied Optics **60**, D15–D32 (2021).
23. D. Dai, Z. Wang, J. F. Bauters, M.-C. Tien, M. J. Heck, D. J. Blumenthal, and J. E. Bowers, "Low-loss silicon nitride arrayed-waveguide grating (de) multiplexer using nano-core optical waveguides," Optics express **19**, 14130–14136 (2011).
24. M. K. Smit and C. Van Dam, "Phasar-based wdm-devices: Principles, design and applications," IEEE Journal of Selected Topics in Quantum Electronics, 2 (2) (1996).
25. S. Mechels, K. Takada, and K. Okamoto, "Optical low-coherence reflectometer for measuring wdm components," IEEE Photonics Technology Letters **11**, 857–859 (1999).
26. K. Okamoto, *Fundamentals of optical waveguides* (Academic press, 2010).
27. T. Zhu, Y. Hu, P. Gatkine, S. Veilleux, J. Bland-Hawthorn, and M. Dagenais, "Ultrabroadband high coupling efficiency fiber-to-waveguide coupler using Si_3N_4/SiO_2 waveguides on silicon," IEEE Photonics Journal **8**, 1–12 (2016).
28. Z. Yao, Y. Wan, Y. Zhang, X. Ma, and Z. Zheng, "Broadband high-efficiency triple-tip spot size converter for edge coupling with improved polarization insensitivity," Optics Communications **475**, 126301 (2020).
29. B. Bhandari, C.-S. Im, K.-P. Lee, S.-M. Kim, M.-C. Oh, and S.-S. Lee, "Compact and broadband edge coupler based on multi-stage silicon nitride tapers," IEEE Photonics Journal **12**, 1–11 (2020).
30. Y. Hu, "Ultra-low-loss silicon nitride waveguide gratings and their applications in astrophotonics," Ph.D. thesis, University of Maryland, College Park (2020).
31. J. Zhan, Y. Zhang, W.-L. Hsu, S. Veilleux, and M. Dagenais, "Design and implementation of a si 3 n 4 three-stigmatic-point arrayed waveguide grating with a resolving power over 17,000," Optics Express **31**, 6389–6400 (2023).
32. S. Yuan, J. Feng, Z. Yu, J. Chen, H. Liu, Y. Chen, S. Guo, F. Huang, R. Akimoto, and H. Zeng, "Silicon nanowire-assisted high uniform arrayed waveguide grating," Nanomaterials **13**, 182 (2022).